

AD-A147 434

AN OPTICAL AND MASS SPECTROMETRIC STUDY OF THE
ALUMINUM-OXYGEN FLAME(U) AIR FORCE ROCKET PROPULSION
LAB EDWARDS AFB CA D P WEAVER ET AL. AUG 84

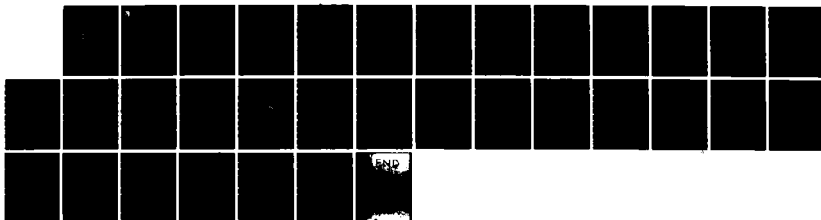
1/1

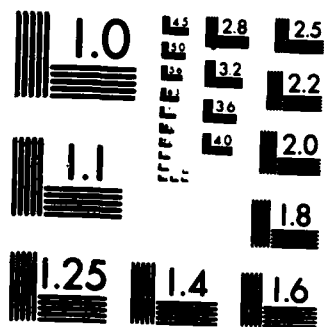
UNCLASSIFIED

AFRPL-TR-84-053

F/G 21/2

NL







AFRPL TR-84-053

AD:

1.2

Final Report
for the period
2 December 1977 to
30 August 1981

An Optical and Mass Spectrometric Study of the Aluminum-Oxygen Flame

August 1984

Authors:
David M. Mann
David P. Weaver

Approved for Public Release

Distribution unlimited. The AFRPL Technical Services Office has reviewed this report, and it is releasable to the National Technical Information Service, where it will be available to the general public, including foreign nationals.

Air Force Rocket Propulsion Laboratory

Air Force Space Technology Center
Space Division, Air Force Systems Command
Edwards Air Force Base,
California 93523

AD-A147 434


DNC FILE COPY

NOTICE

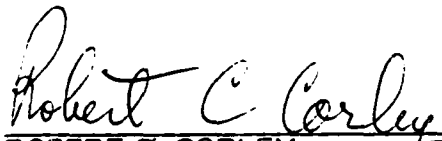
When U.S. Government drawings, specifications, or other data are used for any purpose other than a definitely related Government procurement operation, the fact that the Government may have formulated, furnished, or in any way supplied the said drawings, specifications, or other data, is not to be regarded by implication or otherwise, or in any way licensing the holder or any other person or corporation, or conveying any rights or permission to manufacture, use, or sell any patented invention that may be related thereto.

FOREWORD

The work reported herein was carried out under the technical direction of project managers David M. Mann and David P. Weaver. The project was performed under JON 2308MIUB from 2 December 1977 to 20 August 1981. The report has been reviewed and is released in accordance with the distribution statement on the cover and on the DD Form 1473.




DAVID P. WEAVER
Project Manager



ROBERT C. CORLEY
Chief, Aerothermochemistry Branch

FOR THE DIRECTOR



ROBERT L. GEISLER
Deputy Chief, Propulsion Analysis Division

REPORT DOCUMENTATION PAGE

1a. REPORT SECURITY CLASSIFICATION UNCLASSIFIED			1b. RESTRICTIVE MARKINGS	
2a. SECURITY CLASSIFICATION AUTHORITY			3. DISTRIBUTION/AVAILABILITY OF REPORT Approved for Public Release; Distribution Unlimited	
2b. DECLASSIFICATION/DOWNGRADING SCHEDULE				
4. PERFORMING ORGANIZATION REPORT NUMBER(S) AFRPL-TR-84-053			5. MONITORING ORGANIZATION REPORT NUMBER(S)	
6a. NAME OF PERFORMING ORGANIZATION Air Force Rocket Propulsion Laboratory		6b. OFFICE SYMBOL (If applicable) DYCR	7a. NAME OF MONITORING ORGANIZATION	
6c. ADDRESS (City, State and ZIP Code) Stop 24 Edwards AFB CA 93523			7b. ADDRESS (City, State and ZIP Code)	
8a. NAME OF FUNDING/SPONSORING ORGANIZATION		8b. OFFICE SYMBOL (If applicable)	9. PROCUREMENT INSTRUMENT IDENTIFICATION NUMBER	
8c. ADDRESS (City, State and ZIP Code)			10. SOURCE OF FUNDING NOS.	
			PROGRAM ELEMENT NO. 61102F	PROJECT NO. 2308
			TASK NO. M1	WORK UNIT NO. UB
11. TITLE (Include Security Classification) AN OPTICAL AND MASS SPECTROMETRIC STUDY OF THE.				
12. PERSONAL AUTHOR(S) Weaver, D. P.; Mann, D. M.				
13a. TYPE OF REPORT Final	13b. TIME COVERED FROM 77/12/02 TO 81/8/30	14. DATE OF REPORT (Yr., Mo., Day) 84/08	15. PAGE COUNT 32	
16. SUPPLEMENTARY NOTATION less than, less than or =				
17. COSATI CODES			18. SUBJECT TERMS (Continue on reverse if necessary and identify by block number)	
FIELD	GROUP	SUB. GR.	Aluminum Oxide, Mass Spectrometry, Aluminum Oxygen Combustion, UV Spectra Visibility, Al_2O_3 Molecule, Particle Temperature.	
17	08			
20	05			
19. ABSTRACT (Continue on reverse if necessary and identify by block number) <p>Aluminum oxide particulates are major contributors to aluminized propellant solid rocket stability and two-phase performance losses and are also chief contributors to the visible and infrared exhaust signatures. These particulates result from the combustion of elemental aluminum. A basic research program is being conducted at the Air Force Rocket Propulsion Laboratory (AFRPL) to investigate the formation mechanisms of such particles in a controlled laboratory environment.</p> <p>A high temperature flow reactor has been used in a series of experiments to look at overall rates and identify global mechanisms. Identification of the major aluminum oxide species has been made mass spectroscopically, while initial particle formation has been inferred from the UV/visible spectra. Identification of Al_nO_m species with $0 \leq n, m \leq 2$ has been made. A mass peak at 102 Atomic Mass Units (AMU) has been ascribed to the previously unobserved gas phase Al_2O_3 molecule. The UV/visible spectra from Al_2O_3 flame zone are dominated by a contin-</p>				
20. DISTRIBUTION/AVAILABILITY OF ABSTRACT UNCLASSIFIED/UNLIMITED <input checked="" type="checkbox"/> SAME AS RPT. <input type="checkbox"/> DTIC USERS <input type="checkbox"/>			21. ABSTRACT SECURITY CLASSIFICATION	
22a. NAME OF RESPONSIBLE INDIVIDUAL David P. Weaver			22b. TELEPHONE NUMBER (Include Area Code) (805) 277-5656	22c. OFFICE SYMBOL AFRPL/DYCR

Block 11. ALUMINUM - OXYGEN FLAME (U).

Block 19. ν_{um} . This emission has been attributed to incandescence of newly nucleated alumina particles. The effective temperatures (T_p) of these particles has been found to lie in the range 1960 T_p 2250 K (ambient gas temperature is 800 K). This temperature has been shown to be consistent with the heat flux produced by condensing Al_2O_3 species. Rates for the bimolecular reactions leading to Al_2O_3 have been inferred from the data. Following nucleation and growth to approximately 10 nm diameter, alumina particulates are observed to grow by agglomeration into 0.3- μm clusters.

TABLE OF CONTENTS

<u>Chapter</u>		<u>Page</u>
1	Introduction	1
2	Experimental Apparatus	4
3	Optical Data	9
4	Mass Spectrometric Data	11
5	Results and Analysis	16
5.1	Particulate Emission	16
5.2	Al/O ₂ Kinetics	19
5.3	Particle Agglomeration	21
6	Conclusions	22
	References	24

Approved For

by

Signature

Date

Initial

Final

A1

List of Figures

<u>Figure</u>		<u>Page</u>
1	Schematic illustration of combustion of an aluminum droplet	2
2	Experimental arrangement	5
3	Aluminum vapor source	6
4	Emission spectrum of aluminum-oxygen flame	10
5	Mass spectra obtained from aluminum-oxygen flame	13
6	Relative mass intensities as a function of aluminum concentration: $p = 307 \text{ Pa}$ (2.3 Torr), $T_{\text{gas}} = 800^\circ\text{K}$	14
7	Relative mass intensities as a function of pressure at $T_f = 1320^\circ\text{K}$	14
8	Relative mass intensities as a function of oxygen flow rate at $T_f = 1473^\circ\text{K}$ and $P = 133 \text{ Pa}$ (1 Torr)	15
9	Relative mass intensities as a function of oxygen flow rate at $T_f = 1473^\circ\text{K}$ and $P = 307 \text{ Pa}$ (2 Torr)	15
10	Normalized emission intensity	17
11	Relative mass intensities as a function of oxygen flow rate at $T_f = 1473^\circ\text{K}$ and $P = 133 \text{ Pa}$ (1 Torr) with comparison with computation	21
12	Relative mass intensities as a function of oxygen flow rate at $T_f = 1473^\circ\text{K}$ and $P = 307 \text{ Pa}$ (2 Torr) with comparison with computation	22

List of Tables

<u>Table</u>		<u>Page</u>
1	Aluminum oxide species	3
2	Aluminum/oxygen reactions	3
3	Mass spectrometric data summary	12
4	Aluminum oxide reactions	20

1. INTRODUCTION

This report describes the results of an in-house research program conducted at AFRPL. These studies are designed to identify the mechanisms and determine the kinetics of metal oxide formation; especially as they relate to the production of aluminum oxide (Al_2O_3) particulates during the combustion of aluminized solid propellants. The mechanisms and kinetic rates will be incorporated into improved descriptions of aluminum droplet combustion and oxide condensation which, in turn, are key elements in predictions of propellant combustion, motor performance and plume signatures.

The combustion of an aluminum particle in the oxidizer-rich gases above the propellant surface is a topic of intense current interest and considerable controversy. The schematic of particle combustion shown in Fig. 1 will serve to illustrate the major processes occurring. At a considerable distance from the particle, the ambient gases are oxidizer rich. At the particle surface, convective, radiative, and heterogeneous reaction mechanisms supply heat to the particle resulting in increased aluminum vapor pressure within the droplet and the buildup of fuel rich species outside of the particle. It should be noted that these species probably do not include pure Al but are more likely an aluminum rich oxide (e.g., Al_2O or AlO). In the "classical" model of metal particle combustion based upon the liquid hydrocarbon droplet model¹, the oxidizer and fuel rich regions meet in a flame zone of finite thickness for finite rate flame kinetics, or zero thickness for infinite rate kinetics. The final, stoichiometric oxide, Al_2O_3 , is produced at the outer edge of the flame zone and eventually condenses. A major modification of the above picture has been proposed by Gremyachkin, et. al.² The primary new assumption is that the reactions leading to Al_2O_3 particulate formation are slow compared to diffusion rates. This leads to a droplet that burns by the direct, heterogeneous reaction of ambient oxidizer at the particle surface and Al_2O_3 formation, with its accompanying high heat release, occurring at a large distance from the particle. The critical dependence of both models on assumed mechanisms for gas phase aluminum oxide reactions has motivated the present work to focus on those initial gas phase reactions which lead to particulate alumina.

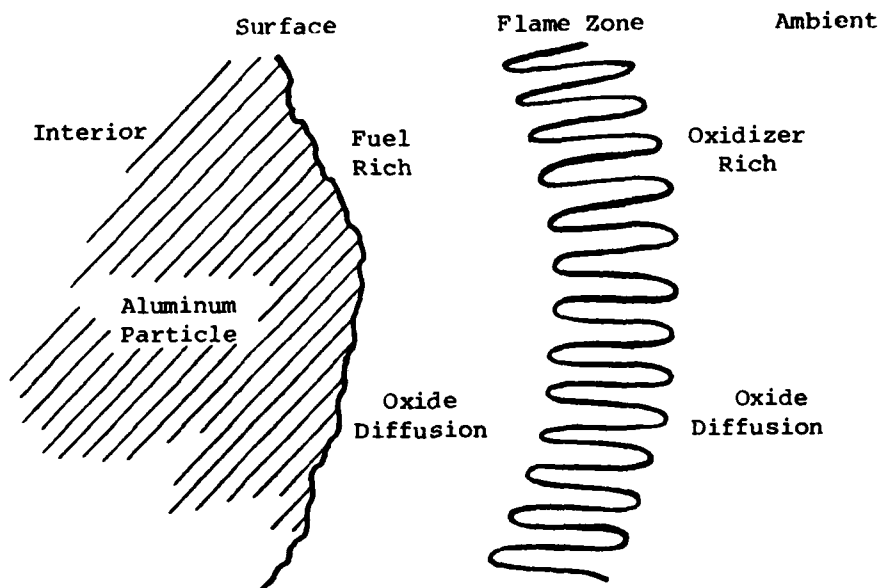


Fig. 1. Schematic Illustration of Combustion of an Aluminum Droplet.

Gas phase oxides of aluminum exist in a variety of compositions from the metal rich Al_2O to the oxygen rich AlO_2 form. These are shown in Table 1 along with their heats of formation as determined from mass spectrometrically measured vapor pressure data.³ Although the gas phase species Al_2O_3 has not been reported in the literature, an estimate of its heat of formation has been included in Table 1 together with a value for liquid Al_2O_3 for comparison. With such a range of oxide compositions possible, the reaction path eventually leading to particulate Al_2O_3 is likely to involve a sequence of steps during which the stoichiometer is changed from metal rich to the final Al_2O_3 composition. The first five reactions in Table 2 are possible bimolecular aluminum oxide reactions leading to the production of the known, gas phase oxide species. Once the gas phase oxides are present, the formation of Al_2O_3 is difficult. Since the gas phase Al_2O_3 molecule has not been previously reported, a scheme has been proposed⁵ for forming a macromolecule with the overall stoichiometry Al_2O_3 from the polymerization of a large number of AlO

molecules and the eventual release of Al. Of course, assuming the presence of a single Al_2O_3 molecule greatly simplifies the problem. The last group of reactions shown in Table 2 reflect the large number of possibilities in direct Al_2O_3 formation. It should be pointed out that only the first two reactions in Table 2 have been reported.⁶

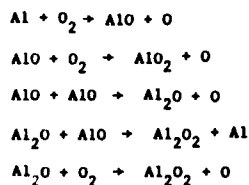
TABLE 1. Aluminum Oxide Species

Species (Gas Phase)	H_{f298} (kcal/mole)	Method
Al	78 ± 0.9	Vapor Pressure Data ⁽³⁾
AlO	16 ± 3.0	Vapor Pressure Data ⁽³⁾
Al_2O	-33 ± 2.0	Vapor Pressure Data ⁽³⁾
AlO_2	-44 ± 2.0	Vapor Pressure Data ⁽³⁾
Al_2O_2	-113 ± 2.0	Vapor Pressure Data ⁽³⁾
Al_2O_3	-198	Estimate ⁽³⁾
Al_2O_3 (Liquid)	373	Extrapolation from Solid ⁽⁴⁾

Note 3:
Note 4:

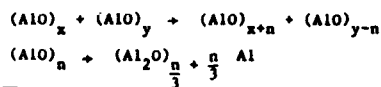
TABLE 2. Aluminum/Oxygen Reactions

CONVENTIONAL

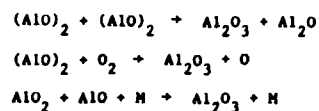


ALUMINA PRODUCING

POLYMERIZATION



DIRECT



In view of the complex and uncertain nature of the Al/O_2 reaction system and the importance of Al_2O_3 formation, the work described below focused on a study of the "simple" Al/O_2 flame and an investigation of the gas-phase mechanisms leading to Al_2O_3 . Subsequent sections of this report deal with the experimental apparatus and general operational concerns (Section 2), a discussion of the experimental conditions used and data obtained (Section 3), analysis and interpretation of the data (Section 4) and conclusions and recommendations (Section 5).

2. EXPERIMENTAL APPARATUS

In a solid propellant rocket motor chamber, operating at pressures from 2×10^6 to 2×10^7 Pa (300 to 3,000 psi), the flame zone around a burning particle could be on the order of a few tens of nanometers in thickness. To study intermediate reactions in such a region is difficult. Accordingly, it was decided to work at subatmospheric pressure using a rapidly flowing reaction system which allows spatial separation of even fast reactions. In addition to the fast flow reactor technique, mass spectrometric detection of reaction products was considered essential for identification of intermediate species. Optical spectroscopy was also required for identification of those few species (Al and AlO) for which spectral data exists.

An overall schematic of the apparatus is shown in Fig. 2. In operation, aluminum vapor was entrained in an argon carrier gas in the furnace section. Upon exiting the furnace, it was immediately mixed with oxygen. The reacting mixture then flowed towards the mass spectrometer inlet. A minute fraction of the reaction products entered the inlet; the remainder was pumped away. At the mass spectrometer inlet, ports were provided for optical measurements and thermocouple or other probe access.

Due to the high reactivity of aluminum vapor, a special furnace was constructed to reduce the possibility of aluminum attack on the tungsten heater winding and heat shields. The design shown in Fig. 3 was similar to those developed at the University of California, Santa Barbara,⁷ but incorporated extensive use of alumina as the primary heat shielding material.

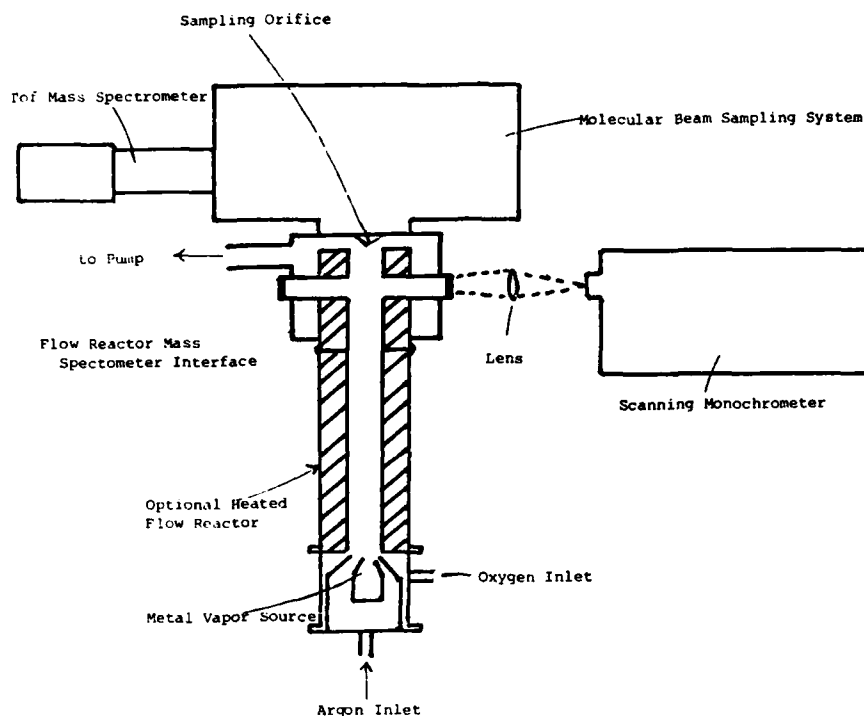


Fig. 2. Experimental Arrangement.

Earlier versions used molybdenum and tantalum heat shields which were severely eroded by aluminum attack in a few hours of operation. The furnace heater was formed from stranded tungsten wire clamped to water-cooled, copper electrodes which were connected to the water-cooled, 10-cm diameter base by ceramic-to-metal insulators. A 7.5-cm long, 2-cm inside diameter (i.d.) alumina tube, closed on one end, formed both the crucible for aluminum evaporation, and a chimney to direct the argon flow. Argon carrier gas was admitted to the bottom of the furnace, flowed around the heater winding and entered the chimney through slots in the tube side. The argon mixed with vaporizing aluminum and exited the chimney as a low pressure jet. Oxygen was added to the emerging jet 0.2 cm from the chimney exit through a manifold of six 0.5-mm tubes placed normal to the jet.

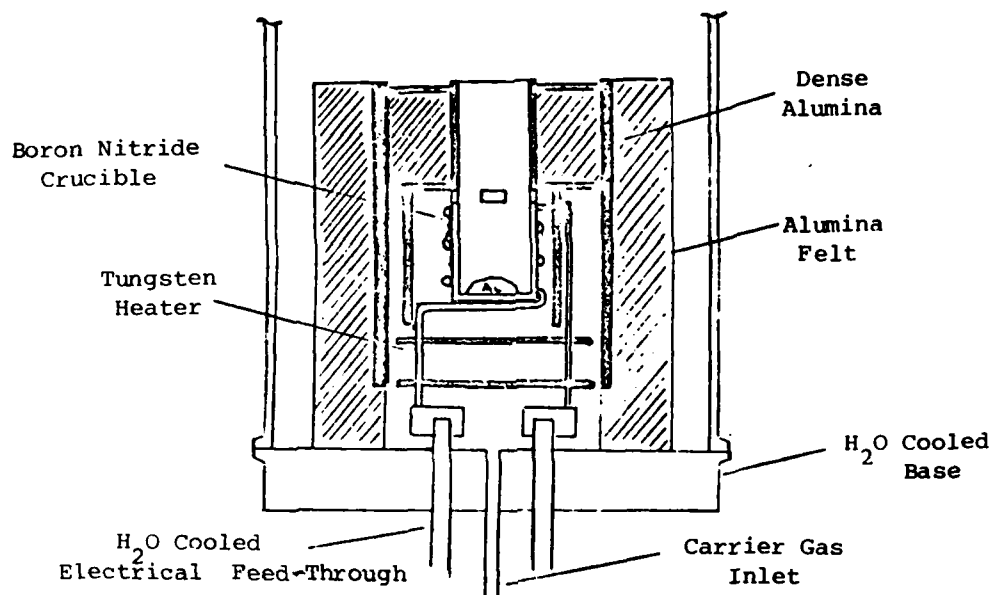


Fig. 3. Aluminum Vapor Source.

The furnace was operated from a high current DC power supply. Due to the large thermal mass, temperature stability was quite good ($\pm 2^\circ\text{K/hr}$) once nominal operating temperature was attained. A major uncertainty in the experimental data is the inaccuracy in the furnace temperature determination. A thermocouple was routinely used to measure the crucible external wall temperature. On several occasions, thermocouple values were compared with the readings taken by an optical pyrometer sited on the inside of the crucible. After making appropriate emissivity and transmittance corrections, these values were consistently found to track each other, with the pyrometer being 30°K higher. Due to the difficulty in the measurement, ± 20 to 30°K probably represents the accuracy of quoted temperatures.

Apart from the furnace, the fast flow reactor consisted of a removable 30-cm long, heated flow tube and the interface section which mated the flow reactor to the mass spectrometer, providing optical, probe and pumping ports. The heated flow tube was a 30-cm section of 4-cm i.d. high purity alumina tube

with an external spiral-wound tungsten wire heater. It was mounted, with additional alumina insulation, in a water-jacketed, 20-cm diameter flanged section of stainless steel tubing which fit directly above the furnace. The flow tube power was provided from a separate DC supply and was found capable of sustained operation at 1800°K. Use of the flow tube gave a total reaction distance of 38 cm from oxidizer inlet to mass spectrometer entrance. At the flow rates and pressures used in the experiments, this distance was too long to permit intermediate species observation. Thus, the flow tube section was only used in observations of particle agglomeration. The majority of data was obtained using the furnace directly mounted to the interface section, giving an 8-cm reaction length.

Two versions of the interface section were fabricated: one entirely from stainless steel and one with an alumina interior. The exterior was octagonal, allowing for easy attachment of two pumping ports, four optical windows, pressure taps, probe feed-thrust, etc. The interior diameter of this section was 25 cm. The interior of the interface was a straight tubular section 20-cm outside diameter (o.d.) 0.5 cm thick, which extended from the top of the furnace (or flow tube, if used) to within 1 cm of the flange holding the mass spectrometer entrance cone. The area between this inner tube and the interface chamber outer wall formed a plenum chamber. In operation, the flow impinged normal to the mass spectrometer flange, turned, and was pumped out through the plenum. Pump lines, 5.0-cm i.d., were connected directly to the plenum via flow control valves to a 63 liter/sec (135 ft³/min) mechanical pump. The interface optical ports were 3.5 cm in diameter and were centered 2 cm upstream of the mass spectrometer sampling inlet. Steady, uniform flow patterns were observed under all flow conditions with little evidence of substantial recirculation in the region between the approximately 2-cm diameter reacting jet and interface inner wall. In the second version, the stainless steel interior sections were replaced with alumina to reduce the convective heat load on external o-ring seals.

Gaseous flow rates were measured using standard rotameters and controlled through needle valves mounted on the furnace section. Reaction pressures were determined using a capacitance manometer reading the interface interior pressure.

The molecular beam-mass spectrometer consisted of a three stage, differentially pumped sampling train which provided a well-collimated beam for detection by the time-of-flight mass spectrometer. The entrance orifice was a 0.2-mm opening at the apex of a 0.5-mm thick spun rhodium cone. The cone was attached to a water-cooled flange. The chamber behind the entrance orifice was evacuated by a 25-cm (10-in) diameter oil diffusion pump. Approximately 2 cm from the entrance orifice, a stainless steel skimmer cone with a 0.2-mm i.d. opening further defined the beam. The skimmer chamber was pumped by a 15-cm (6-in) oil diffusion pump. A final 0.5-mm by 3-mm collimating orifice, 6 cm from the skimmer, led to the mass spectrometer ionizer. An oil-free turbo-molecular pump was used in this last section to reduce oil contamination in the ionizer region. Details of this system have been previously published.⁸ In operation, with a 1.2 kPa (10 torr) pressure in front of the entrance orifice, pressures of about 10^{-3} , 10^{-4} and 10^{-6} Pa (10^{-5} , 10^{-6} and 10^{-8} torr) were maintained in the 25-cm, 15-cm, and ionizer stages, respectively. The 0.2-mm entrance orifice was larger than usually encountered in similar systems but was chosen as the best compromise between high pressure operation (favoring small orifices) and nozzle clogging problems (favoring large orifices). As a result, mass intensity versus pressure traces were found to be linear up to 40 torr where they started to flatten out due to excessively high 25-cm chamber pressure and departure from molecular beam conditions.

The mass spectrometer was a Bendix Model MA-3 time-of-flight unit, which operated at an internal rate of 30 kHz. To get maximum signal-to-noise ratio, 2 to 3 minutes were used to obtain a mass spectrum from 14 to 120 atomic mass units (AMU). In early experiments, the mass spectrometer ion current was detected by a picoammeter, the output of which was displayed on a strip chart recorder. Mass locations were measured from positions of O and Ar peaks using the quadratic dependence of mass number on scan time characteristic of time-of-flight mass spectrometers. Later experiments employed a data system which, after suitable calibration, digitally recorded peak intensity as a function of mass number.

Even with a turbomolecular pump and LN₂ cold-trap in the mass spectrometer stage, hydrocarbon peaks severely contaminated the early spectra.

A major factor was apparently oil contamination getting in the ionizer during the system shut downs performed every weekend (in anticipation of power outages or other calamities). Finally, automatic gate valves were added in all three sections to isolate the pumps in the event of power failure and the system was continuously pumped for several weeks. Hydrocarbon background spectra were reduced to less than 1/100 their former value. Additional water flow and thermal overload protection circuits were added to the control circuitry and the system was continuously pumped during the rest of the program.

Sensitivity, or more precisely, signal to background ratio, of the molecular beam mass spectrometer was found to be a rather critical function of beam alignment. The following procedure evolved as an easy solution. An He-Ne laser was used to align the skimmer and entrance orifices to the mass spectrometer ionizer. By replacing the skimmer flanges with a quartz optical flat with etched cross hairs, the laser beam could be centered in the ionizer, made parallel to the molecular beam axis (perpendicular to the skimmer flange) and centered at the skimmer location. Removing the quartz plate, installing the skimmer and entrance orifices completed the alignment.

Optical spectra were obtained using a 0.5-m focal length, scanning monochromator and S-5 surface photomultiplier detector. A mirror-lens relay system was used to optically position the entrance slit normal to the flow direction for maximum spatial resolution. A conventional picoammeter/chart recorder combination was used for output display. Corrections for spectrometer/detection response were determined from spectra taken using a calibrated, standard lamp positioned inside the chamber at the flow center line.

3. OPTICAL DATA

It was not possible to obtain complementary optical and mass spectrometric data. The optical detection system had rather low sensitivity which required high furnace temperatures and flow rates in order to produce sufficient radiant intensity from the flame. Under such conditions, mass spectrometer operation was only feasible for a few seconds due to rapid

clogging of the sampling orifice. As will be shown below, the spectra in the 300 to 600 nm wavelength range were dominated by continuum emission except for atomic aluminum and AlO emission. Therefore, it was decided that pursuing the mass spectrometer data was more fruitful and only a short series of experiments was devoted to measuring optical spectra.

Figure 4 shows typical emission spectra at the aluminum/oxygen flame. The furnace temperature (T_F) was 1600°K with an argon flow rate of $56\text{ cm}^3/\text{sec}$ (STP). The upper trace is for an oxygen flow so low that a reliable value

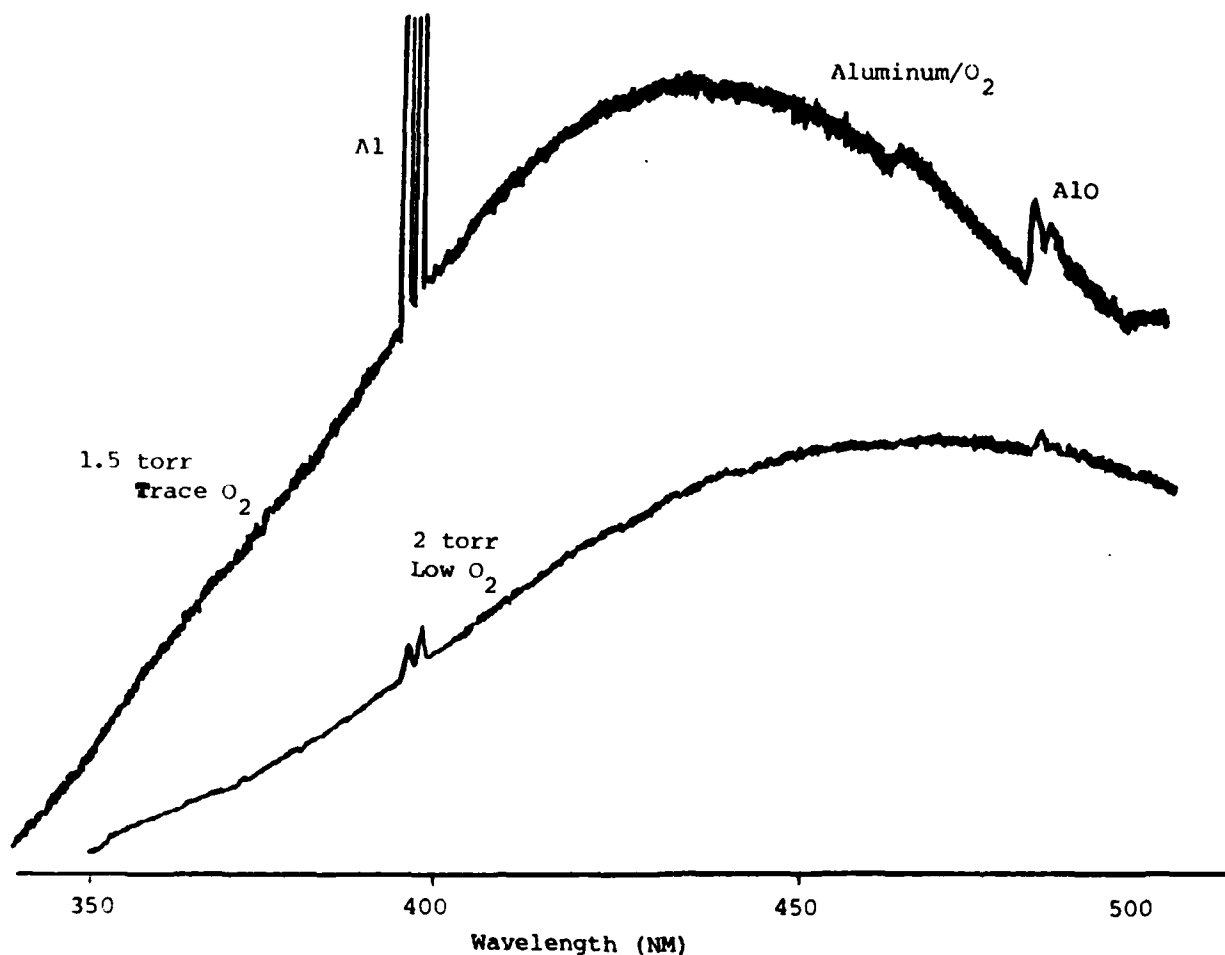


Fig. 4. Emission Spectrum of Aluminum-Oxygen Flame.

could not be read on the rotameter (less than $0.05\text{-cm}^3/\text{min.}$) The lines at 394 and 396 nm are the atomic aluminum resonance lines. The features from 480 to 500 nm are the $\text{AlO} (\text{B}^2 \Sigma^+ + \text{x}^2 \Sigma^-)$ transition. At slightly higher pressure and oxygen flow, the spectrum changes dramatically as shown in the lower trace. There is a marked reduction in both atomic and molecular components and an apparent shift in the continuum. However, when the detection system response is used to correct the spectra, the difference is not as large as Fig. 4 would indicate (see Section 5). There is a possibility that there is some underlying continuum due to molecular species which contributes to the upper curve.

4. MASS SPECTROMETRIC DATA

As noted above, the range of experimental conditions suitable for mass spectrometer operation was limited by the need to reduce orifice clogging and nonlinear behavior at high sampling pressure. Table 3 gives the range of furnace temperature, total pressure and oxygen flow rate used in these studies. Total argon flow rate was held fixed at $38.8 \text{ cm}^2/\text{sec}$ at standard temperature and pressure (STP). In the course of a typical, several hour experiment, the total molecular beam intensity would gradually decay even with reduced furnace temperatures. This was inferred from monitoring the argon mass peak at 40 AMU and attributed to orifice clogging. To facilitate comparisons at different times, all data were normalized to the argon peak. No attempt was made to absolutely calibrate the mass peak intensities. All values were considered relative.

Figure 5 shows a representative scan covering the range from 30 to 110 AMU. The argon 40 peak dominates, followed by oxygen (O_2) at 32 AMU and the several aluminum oxide species. All of these aluminum oxides have been observed previously except for the peak at 102 AMU which is expected to be Al_2O_3 . The peak at 102 AMU was apparently not an impurity as it was only observed in the presence of both aluminum and oxygen. It must be an Al_2O_3 monomer or, at least, a multiply ionized n-mer of charge/mass ratio consistent with its detection at 102 AMU.

Initial reactions were studied at low pressures and low oxygen flow. Under these conditions, variation of furnace temperature produced a variation

TABLE 3. Mass Spectrometric Data Summary.
Argon Flow Rate - 38.8 cm³/sec

Temperature (°K)	Pressure		O ₂ Flow (cm ³ /sec)
	(Pa)	(torr)	
1223	172	1.29	0.18
	307	2.30	0.50
1320	172	1.30	0.18
	307	2.30	0.50
1373	172	1.29	0.50
			0.10
	307	2.30	0.50
			1.25
1423	307	2.30	0.50
			1.25
1473	133	1.00	0.01
			0.65
	181	1.36	0.03
	1330	10.00	0.03
	2670	20.00	0.03
1523	188	1.41	0.24
			0.68
	267	2.00	1.47
	1330	10.00	0.24
			0.68
1573	267	2.00	1.47

in aluminum vapor pressure which was still very much less than the oxygen concentration. Figure 6 shows the atomic aluminum and AlO relative intensities. Of the range of mass spectrometer conditions covered, these come closest to those used to obtain the optical spectra of Figure 4. Vapor pressures are calculated using published data for the corresponding furnace temperature.⁹

Figure 7 summarizes the data obtained as a function of pressure under conditions of constant furnace temperature and oxygen flow. Note that these intensities are not absolute; thus, only the trend for each species is relevant. (The concentration of O₂ is several orders of magnitude above the other species shown.)

Figures 8 and 9 illustrate an interesting anomaly which occurred when a particular furnace crucible was repeatedly used. For the first few hours of

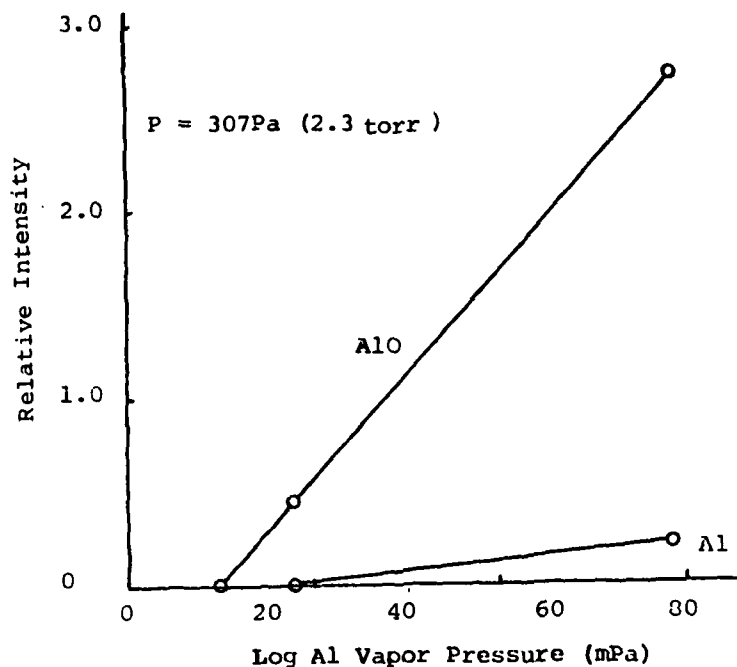


Fig. 6. Relative Mass Intensities as a Function of Aluminum Concentration: $p = 307 \text{ Pa (2.3 torr)}$, $T_{\text{gas}} = 800^\circ \text{K}$.

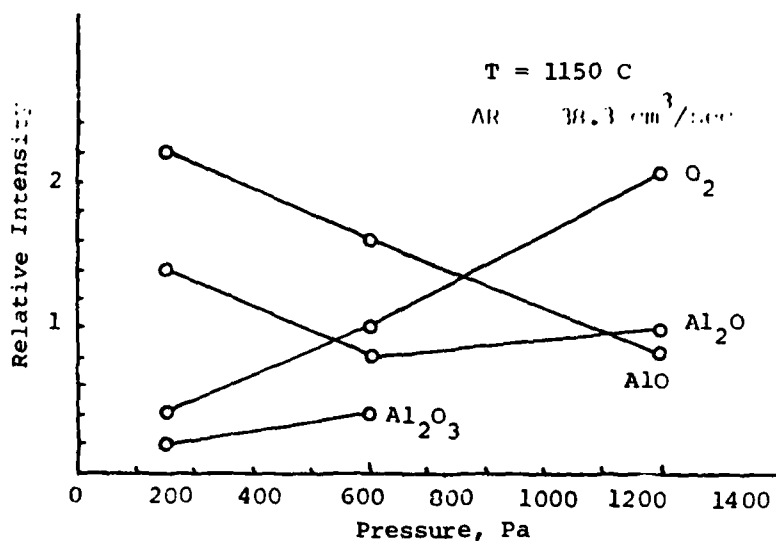


Fig. 7. Relative Mass Intensities as a Function of Pressure at $T_f = 1320^\circ \text{K}$.

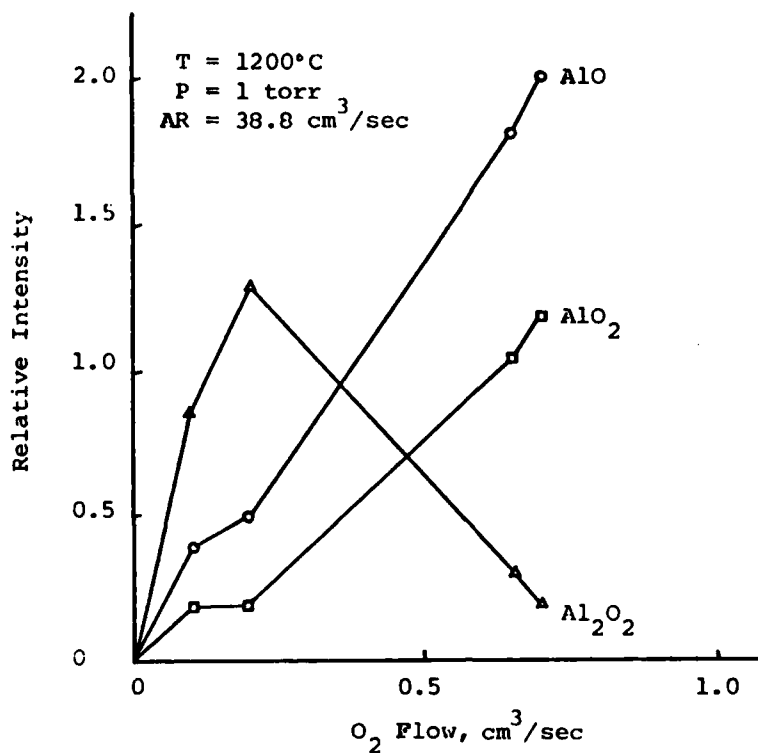


Fig. 8. Relative Mass Intensities as a Function of Oxygen Flow Rate at $T_f = 1473^{\circ}\text{K}$ and $P = 133 \text{ Pa}$ (1 torr).

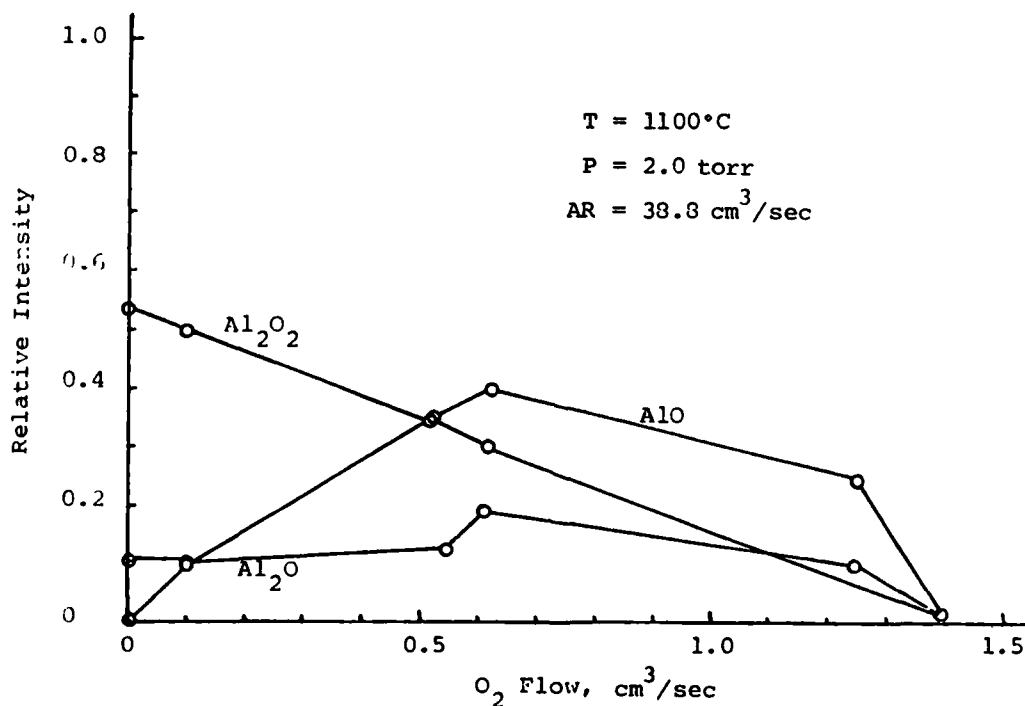


Fig. 9. Relative Mass Intensities as a Function of Oxygen Flow Rate at $T_f = 1473^{\circ}\text{K}$ and $P = 307 \text{ Pa}$ (2 torr).

5. RESULTS AND ANALYSIS

5.1 PARTICULATE EMISSION

The most striking feature of all of the optical data is the dominant continuum. Similar continua have been associated with upper atmosphere trimethylaluminum releases and ascribed¹¹ to emission from aluminum oxide molecular species, specifically AlO. While this possibility cannot be discounted based on the present data, the experimental conditions involved here are quite different. Particularly, optical spectra were most intense at high furnace temperatures, hence high aluminum concentrations, where it was impossible to obtain mass spectral data due to nearly instantaneous clogging of the sampling orifice. That, together with the blue-to-white shift of the radiation with increasing pressure, suggests that the radiation may be from particulates. To determine if this was a possible explanation, the equivalent black body temperature of the continuum was determined and compared with what might be expected for a growing particle in thermal equilibrium.

Using the standard-lamp determined spectrometer response functions, the spectral data were reduced to source intensity spectra as shown in Fig. 10. These have definite characteristics of grey-body emission. Assuming spectrally constant emissivity, the measured intensities at 350 and 400 nm were used in the Wien (short wavelength) approximation to the Planck radiation law to derive equivalent temperatures. Thus,

$$T = C_2 \left(\frac{1}{\lambda} - \frac{1}{\lambda^2} \right) / \ln \frac{N_1 \left(\frac{\lambda_1}{\lambda_2} \right)^5}{N_2}$$

where $C_2 = 1.439 \text{ cm-K}$ and $N_{1,2}$ is the radiation intensity at $\lambda_{1,2}$. The derived temperatures ranged from 1950°K to 2260°K with higher temperatures corresponding to higher flow rates, pressures and furnace temperatures. Additionally, the higher temperature spectra were the only ones to show evidence of molecular AlO emission. The derived temperatures are considerably in excess of the 800 to 1,000°K ambient gas temperatures as measured by a thermocouple probe. In fact they are representative of other measurements of Al/O₂ flame temperatures.¹² Particle temperatures were calculated by

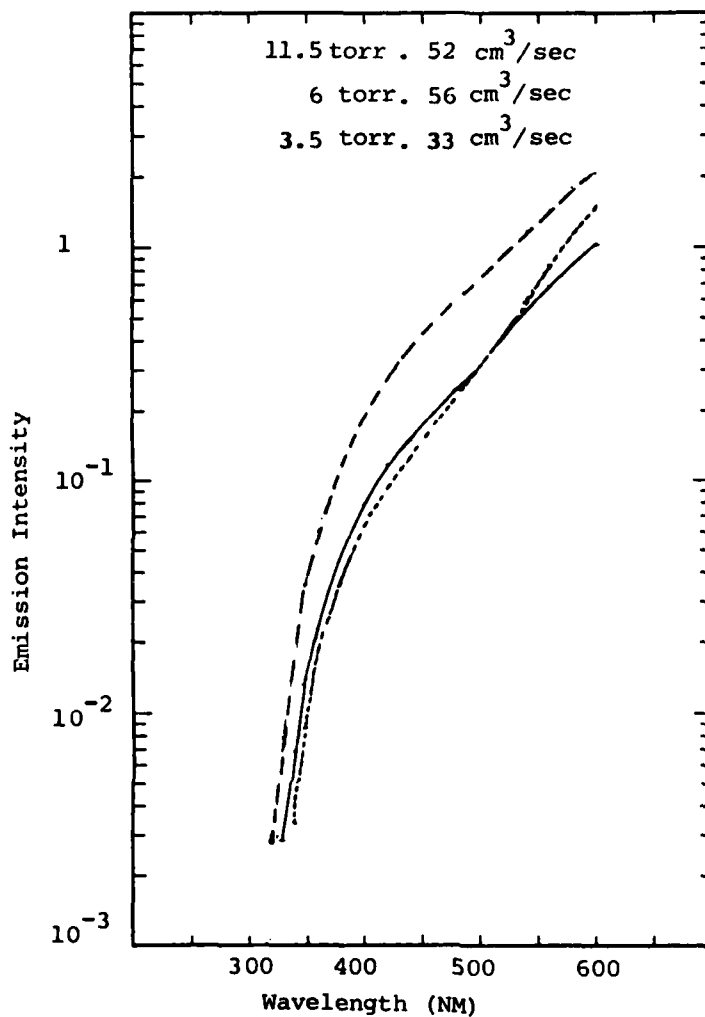


Fig. 10. Normalized Emission Intensity.

calculating the net heat fluxes into and out of the particle. Sub-micron particles, at the pressures used in these experiments, will be in the free-molecular flow regime, i.e. the particle diameter is much less than the gas mean free path. Under that condition, it is straightforward to write down the net heat flux to a particle undergoing a heterogeneous reaction.¹³

$$\begin{aligned} \dot{H} &= \dot{H}(\text{convective}) + \dot{H}(\text{reactive}) - E(\text{radiation}) \\ \dot{H} &= \pi d^2 \alpha_{ta} \left[\frac{1}{4} n^+ v^+ (2KT^+ + U_{int}^+) \right] - \frac{1}{4} n^- v^- (2KT^- + U_{int}^-) \\ &+ \alpha_R \frac{1}{4} n^+ v^+ U_R - E(\text{radiation}). \end{aligned}$$

Where α 's are accommodation coefficients for thermal accommodation (ta) and reaction (R), $1/4 nv$ is the species flux to (+) or away from (-) the particle, T is the particle (P) or gas (o) temperature and U is the internal (int) or reaction (R) energy. This relation may be greatly simplified by noting that the reactive term is much greater than the convective ones, which may be dropped. Since the particle is in equilibrium ($\dot{H} = 0$), the added heat must be lost by radiation.

$$\dot{H}(\text{reactive}) = E(\text{radiation})$$

or

$$\alpha_R \frac{1}{4} n^+ v^+ U_R = \epsilon \sigma (T_p - T_o)^4$$

where ϵ is the particle emissivity, σ is the Stephan-Boltzman constant ($5.67 \times 10^{-5} \text{ erg/sec cm}^2 \cdot \text{K}^4$) and T is the particle (p) or background (o) temperature.

This may be rewritten to express the particle temperature as a function of thermodynamic and radiation parameters. Note that actual particle size no longer appears.

$$T_p = T_o + \left(\frac{\alpha_R n^+ v^+ U_R}{4\epsilon\sigma} \right)^{1/4}$$

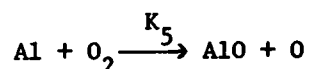
Assuming unity reaction probability, a reactive mole fraction of 10^{-4} , together with particle emissivity¹⁴ of 1.5×10^{-3} gives $T_p = 2,100^\circ\text{K}$, in good agreement with the 1,950 to 2,260°K derived from the spectra.

There are obviously major uncertainties in species concentrations and emissivities. However, the result is not very sensitive to even modest errors. The prediction of a particle temperature in agreement with that determined from the optical spectra gives good support, if not conclusive proof, for the proposition that the continuum is due to particle

incandescence. A similar mechanism has been proposed for radiation from the $\text{Mg} + \text{O}_2$ flame.¹⁵

5.2 Al/O_2 KINETICS

As was mentioned in the introduction, the possible set of aluminum/oxygen reactions is quite large and substantially unknown. Fortunately, the mass spectral data allows a verification of the $\text{Al} + \text{O}_2$ reaction rate obtained optically.¹⁶ Figure 6 shows the observed variation of AlO mass peak intensity with Al vapor pressure. From this data, since $[\text{O}_2] \gg [\text{Al}]$ the reaction rate for



was determined to be $K_5 = 3 \times 10^{-11} \text{ cm}^3/\text{molecule sec}$. This is virtually identical to the literature value of $K_1 = 2.7 \times 10^{-11} \text{ cm}^3/\text{molecule sec}$ reported for this reaction.

Unfortunately, only this initial reaction was found to separate so neatly. Once the initial AlO is formed, the competing routes become quite complex. Accordingly, a set of reactions was sought which could reproduce the measured changes in concentrations of aluminum oxide intermediate species.

The time evolution of aluminum oxide species was modeled using the one-dimensional, constant pressure Generalized Kinetics Analysis Program (GKAP).¹⁶ This program computes the time dependent species concentrations from an initial mixture given reaction rates, temperature and pressure. Aluminum and oxygen reactants were assumed to be fully mixed at the start of the calculation. The reaction set used is given in Table 4. For the first two reactions, the measured rates of Fontijn and Felder^{16, 18} were used. The remainder were set near the gas kinetic limit (Unity reaction probability per collision). While some three-body reactions are included in the set, they were not expected to be very important due to the low pressures and short times represented by the experimental data.

The success of the preliminary reaction rate estimates is shown in Fig. 11 for the prediction of AlO production. The good agreement is not

particularly surprising since the $\text{Al} + \text{O}_2$ reaction is controlling the rate of AlO formation. Figure 12 shows the results of a calculation for the conditions of Fig. 9 which has been done assuming equal initial concentrations of Al_2O_2 and Al_2O . The agreement with the data is reasonably good but certainly fortuitous since no attempt has been made to iterate on the reaction rates to obtain a better fit. Better agreement would probably be realized by increasing the rate of Reaction 12, $\text{Al}_2\text{O}_2 + \text{O}_2 \rightarrow \text{Al}_2\text{O}_3 + \text{O}$, which was the predominant bi-molecular route to the formation of the Al_2O_3 monomer. The behavior of the Al_2O_2 concentration shown in Fig. 2 is typical of an intermediate species on a coupled reaction set.¹⁹

TABLE 4. Aluminum Oxide Reactions.

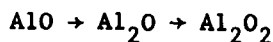
Three Body

1. $\text{O} + \text{O} + \text{M} \rightarrow \text{O}_2 + \text{M}$	$k_1 = 1.6 \times 10^{-53} \text{ T}^{-1} \text{ cm}^6 \text{ molec}^{-2} \text{ sec}^{-1}$
2. $\text{Al} + \text{O} + \text{M} \rightarrow \text{AlO} + \text{M}$	$k_2 = 1.6 \times 10^{-53} \text{ T}^{-1} \exp(-1000/\text{T})$
3. $\text{AlO} + \text{AlO} + \text{M} \rightarrow \text{Al}_2\text{O}_2 + \text{M}$	$k_3 = 8.3 \times 10^{-59} \text{ T}^{-1} \exp(-1000/\text{T})$
4. $\text{Al}_2\text{O}_2 + \text{O} + \text{M} \rightarrow \text{Al}_2\text{O}_3 + \text{M}$	$k_4 = 1.6 \times 10^{-53} \text{ T}^{-1} \exp(-1000/\text{T})$

Two Body

5. $\text{Al} + \text{O}_2 \rightarrow \text{AlO} + \text{O}$	$k_5 = 3 \times 10^{-11} \text{ cm}^3 \text{ molec}^{-1} \text{ sec}^{-1}$
6. $\text{AlO} + \text{O}_2 \rightarrow \text{AlO}_2 + \text{O}$	$k_6 = 3 \times 10^{-13}$
7. $\text{AlO} + \text{AlO} \rightarrow \text{Al}_2\text{O} + \text{O}$	$k_7 = 3 \times 10^{-13}$
8. $\text{AlO}_2 + \text{Al} \rightarrow 2\text{AlO}$	$k_8 = 3 \times 10^{-13}$
9. $\text{Al}_2\text{O} + \text{O}_2 \rightarrow \text{Al}_2\text{O}_2 + \text{O}$	$k_9 = 3 \times 10^{-13}$
10. $\text{Al}_2 + \text{AlO} \rightarrow \text{Al}_2\text{O}_2 + \text{Al}$	$k_{10} = 3 \times 10^{-13}$
11. $\text{Al}_2\text{O}_2 + \text{Al}_2\text{O}_2 \rightarrow \text{Al}_2\text{O} + \text{Al}_2\text{O}_3(\text{g})$	$k_{11} = 3 \times 10^{-13}$
12. $\text{Al}_2\text{O}_2 + \text{O}_2 \rightarrow \text{Al}_2\text{O}_3(\text{g}) + \text{O}$	$k_{12} = 3 \times 10^{-13}$
13. $\text{AlO}_2 + \text{AlO}_2 \rightarrow \text{Al}_2\text{O}_3(\text{g}) + \text{O}$	$k_{13} = 3 \times 10^{-13}$
14. $\text{AlO}_2 + \text{Al}_2\text{O} \rightarrow \text{Al}_2\text{O}_3(\text{g}) + \text{Al}$	$k_{14} = 3 \times 10^{-13}$

Reactions 5, 9, and 10 control the production of Al_2O_2 through the chain of species.



The GKAP program automatically performs a screening process to sort out those reactions which have a minor effect on total species production. Based on this criteria, the three body reactions were ruled out together with Reaction 6, $\text{AlO} + \text{O}_2 \rightarrow \text{AlO}_2 + \text{O}$. However, as was pointed out previously,

the three body reactions may be expected to be much more important at pressures representative of rocket motor chambers.

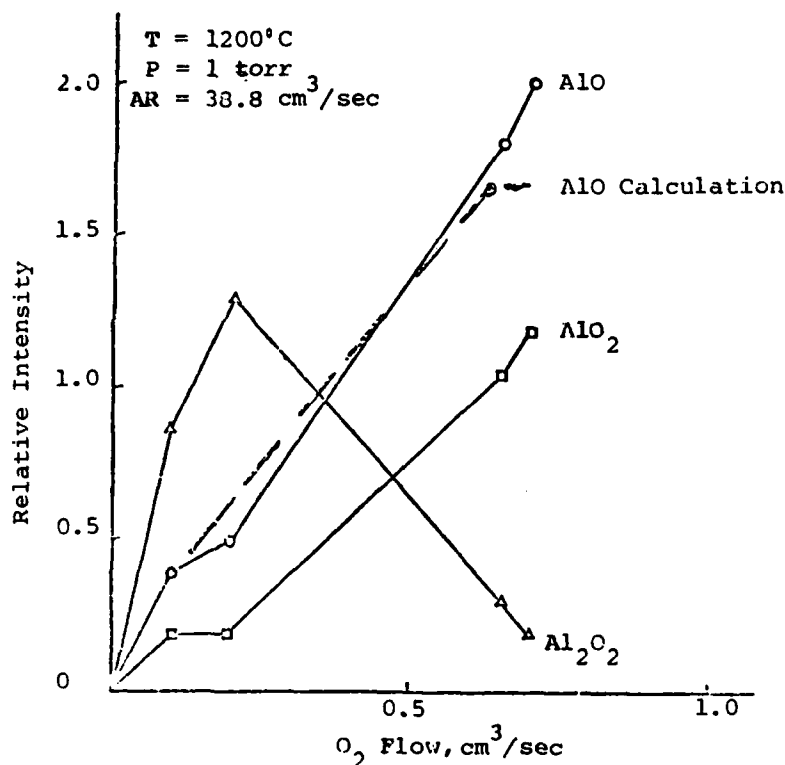


Fig. 11. Relative Mass Intensities as a Function of Oxygen Flow Rate at $T_f = 1473^{\circ}\text{K}$ and $P = 133 \text{ Pa}$ (1 torr) with Comparison with Computation.

5.3 PARTICLE AGGLOMERATION

Scanning electron micrographs of particulates collected on fine, platinum wires at the end of the 30-cm heated flow tube above the flame zone micron-sized aggregates composed of spherical particles of about 10-nm diameter. Similar results have been obtained for carbon vapor condensation²⁰ and fused silica smokes²¹ suggesting a similarity of mechanisms for condensation of these high temperature species. In contrast to the carbon results, the alumina agglomerates do not show the chained structure attributed to particle charge influence.²⁰

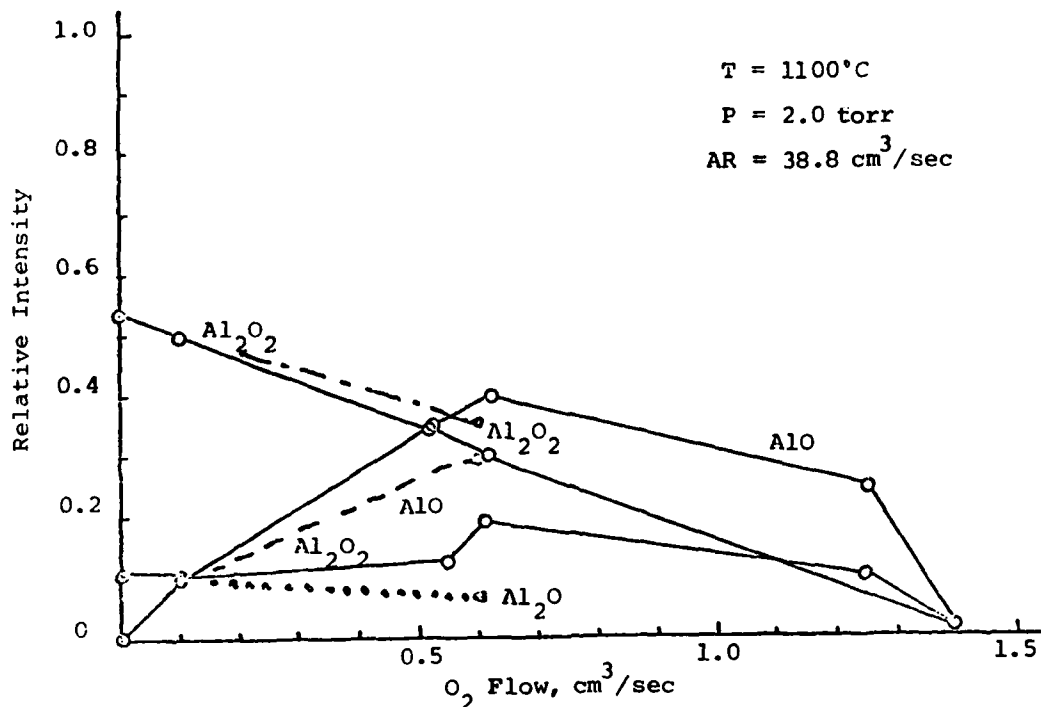


Fig. 12. Relative Mass Intensities as a Function of Oxygen Flow Rate at $T_f = 1473^{\circ}\text{K}$ and $P = 307 \text{ Pa}$ (2 torr) with Comparison with Computation).

6. CONCLUSIONS

The analyses of Section 4 can be combined to form a unified picture of alumina particulate formation as observed during these experiments. The initial set of gas phase reactions proceeds very fast leading to high molecular weight oxides, very probably Al_2O_3 . Initial particle formation is taking place during this period, yielding sub-micron particulates heated to incandescence by their heat of formation.

For a burning aluminum particle, at least in an oxygen atmosphere, the very rapid gas phase kinetic path leading to oxide formation would be expected to give rise to a diffusion controlled combustion process at high pressure. Further, the gas phase formation of particulate oxide should cloud the burning

parent particle in a "halo" of smoke. This is exactly what has been observed to take place in photographic studies of high pressure aluminum combustion. In fact the model also points out major concerns in the interpretation of such observations: (1) size measurements are probably more representative of the oxide cloud than of the parent particle and (2) optically measured parent particle temperatures are probably strongly influenced by the temperature of forming particulates in the cloud.

REFERENCES

1. Glassman, I. and Brzustowski, T., Progress in Astronautics and Rocketry, Academic Press, NY, 1964, pp. 41 - 176.
2. Gremyachkin, V. M., Istratov, A. G., and Leypunskiy, O. I., Arch Thermo in Spalania (USSR), Vol 8, pp 13, 1977.
3. Faber, M., Strivastava, R. D., and Uy, O. M., (Journal of the Chemistry Society Faraday 1.,) Vol 68, p. 249, 1972.
4. Stull, D. R. and Prophet, H., JANNAF Thermochemical Tables, NSRDS -NBS37, Second Edition, 1971.
5. Henderson, C. B., (Combustion, Science and Technology) Vol I, p. 275, 1970.
6. Fontijn, A., Felder, W., and Houghton, J., Sixteenth Symposium (International) on Combustion, The Combustion Institute, 1977.
7. West, J. B., Bradford, R. S., Jr., Eversole, J. D., and Jones, C. R., (Review of Scientific Instruments,) Vol. 46, p. 164, 1975.
8. Goshgarian, B., Selph, C., and O'Pray, J., AIAA Paper 74-1141, Oct 1974.
9. Dushman, S., Scientific Foundations of Vacuum Technique, (Wiley and Sons,) New York, 1962.
10. Porter, R. F., Schissel, P., Inghram, M. G., (Journal of Chemical Physics,) Vol. 23, p. 339, 1955.
11. Kolb, C. E., Gersh, M. E. and Hershback, D. R., (Combustion and Flame,) Vol. 25, p. 31, 1975.
12. Rautenberg, T. H., and Johnson, R. P., Journal Optical Society American, Vol. 50, p. 602, 1960.
13. Hidy, G. M. and Brock, J. R., The Dynamics of Aerocolloidal Systems, Pergamon Press, Oxford, 1970.
14. Plass, G. N., (Applied Optics,) Vol. 3, p. 867, 1964.
15. Markstein, G. H., Ninth Symposium (International) on Combustion, The Combustion Institute, 1962.
16. Fontijn, A., Felder, W. and Houghton, J., (Chemical Physics Letters,) Vol. 27, p. 365, 1974.
17. Nickerson, G. R., Frey, H. M., and Coats, D. E., "GKAP: Generalized Kinetics Analysis Program," Ultrasystems, Inc., Internal Report, 1971.
18. Felder, W. and Fontijn, A. J., (Chemical Physics,) Vol. 64, p 1977, 1976.

19. Kondrat'ev, V. N., Chemical Kinetics of Gas Reactions, Pergamen Press, Oxford, 1964.
20. Mann, D. M., (J. Applied Physics,) Vol. 49, p. 3485, 1978.
21. Ulrich, G. D., Milnes, B. A., and Subramanian, N. S., (Combustion, Science and Technology,) Vol. 14, p. 243, 1976.

END

FILMED

12-84

DTIC